RSC Advances

ROYAL SOCIETY OF CHEMISTRY

www.rsc.org/advances

Two-dimensional Ferromagnetic Iron Crystals Constrained by Graphene Edges : A First Principles Study

Peng Wang, Hongtao Wang[*]*, Wei Yang*

Institute of Applied Mechanics, Zhejiang University, Hangzhou 310027, China

ABSTRACT

Graphene edge, the thinnest and strongest support, may provide necessary constraint in preventing the collapse of two-dimensional (2D) crystals into 3D clusters, as studied by density functional theory (DFT). An epitaxial relation is ensured by the negligible lattice mismatch between the monolayer iron crystal and the zigzag graphene edge. The 1D coherent interfaces suggest new contact prototypes between 2D crystals with different bonding natures. Three different interfacial structures were proposed. The corresponding electronic and magnetic structures are systematically studied by DFT methods. In addition, the lower dimensionality remarkably alters the orbital overlaps, resulting in a large average magnetic moment of 2.68 μ_B per Fe atom. The strong support from the non-magnetic graphene enables the construction of a 2D device prototype.

[*] To whom correspondence should be addressed. Email: htw@zju.edu.cn

I. INTRODUCTION

Dimensionality, as one of the most intriguing factors, bears dramatic consequence on materials' properties, such as the electronic structure,[1-5] magnetic property[6] and chemical reactivity.[7] In 1930s, Landau[8] and Peierls[9] theoretically proved that the long-range order of two-dimensional lattice could not exist at any finite temperature, based on the standard harmonic approximation.[10-12] However, stabilized by the microscopic roughening in 3D space, the recent discovery of graphene has convincingly demonstrated the existence of nearly perfect 2D crystals.[10] Up to date, many compounds have been fabricated into 2D atomic crystals by mechanical exfoliation.[12] Generally, all their bulk counterparts have layered structures, characterized by the strong in-plane bonding and the weak inter-plane van der Waals interaction. Recently, effort has also been devoted to transform non-layered materials into 2D forms. Silicene, a corrugated honeycomb structure, has been epitaxially grown on Ag (111) surfaces with six-fold symmetry.[13, 14] Few-layer metals can be directly deposited onto templates without agglomeration.[15-17] Nevertheless, a 3D substrate must be utilized as an integrated part to support the formation of 2D add-layers. Free-standing crystals in real 2D forms have not been observed or synthesized for these bulk materials. For metals, the difficulty resides in the enormous surface energy, which leads to instantaneous collapse for surface area minimization. In contrast, it is easy to transform a liquid drop into a 2D membrane supported by a thin wire. This inspired us to design a scheme to assemble iron nano-particles into 2D atomic crystals at the graphene edge, which provides the thinnest and strongest

circumferential support.

In this work, we show that monolayer iron crystals can be assembled on graphene edge due to the strong bonding between metal and carbon atoms. Comprehensive density functional theory (DFT) simulations demonstrate the existence of a monolayer iron crystal constrained by graphene edges, which provides sufficient constraint in preventing the collapse of small 2D Fe crystals into 3D close-packing structures. Both the electronic structure and the magnetic property show a strong correlation to the dimensionality. Besides the strong confinement, the in-plane covalent bonding also presents a new 1D contact prototype, which differs from the interfaces in the stacking graphene heterostructure.[18, 19] This prototype may have important applications in spintronics.

II. SIMULATION METHOD

A series of the DFT calculations have been performed by Quantum-Espresso code[20] with an energy cutoff of 60 Ry in the spin-polarized scheme. The self-consistency error is less than 10^{-8} Ry with a Monkhorst-Pack[21] *k*-point mesh of 8×8×2. The ultra-soft pseudo-potentials of RRKJ type[22] are employed with the generalized gradient approximation in the Perdew, Burke, and Ernzerhof parameterization.[23] A denser Monkhorst-Pack grid of 20×20×4 and a Gaussian smearing of 0.01 Ry were used in calculating the density of states. The convergence criteria are that the change in the total energy is less than 10^{-4} Ry between two consecutive steps and all force components on each atom are less than 10^{-3} Ry/Bohr. The interlayer distance is set to 30 Å in order to avoid the inter-plane interaction.

The interfacial strength and the stability were analyzed at finite temperature by quantum chemical molecular dynamics based on the density-functional tight binding (MD/DFTB) method.[24, 25] The DFTB method employs a second-order expansion of the Kohn-Sham total energy with a self-consistent redistribution of Mulliken charges, which enables longer simulations for non-equilibrium dynamics of nano sized clusters.[26, 27] This method has been performed successfully in studying the catalytic effect of nano iron clusters on nucleation and growth of single-walled carbon nanotubes (SWCNT).[26-30] Due to the similarity between graphene and SWCNT, we expect that this MD/DFTB method can catch the essential dynamic behavior of the graphene/iron crystal system at finite temperature. In all simulations, a Monkhorst -Pack grid of 4×4×1 is uniformly sampled in the Brillouin zone. Structure optimization requires the residual force on each atom to be less than 10^{-5} Hartree/Bohr.

III. RESULTS AND DISCUSSION

A. Atomic configuration of a monolayer iron crystal

The chemical inertness of graphene surface induces the least disturbance to the cluster *via* van der Waals interactions. Our recent research shows that the ultrafine Fe clusters have a stable close-packed atomic configuration and a layered structure with the (111) basal plane.[31] The nearest neighbor distance is measured to be 2.7 Å by using the inherently built atomic scale of the C-C bond length of 1.42 Å. The planar geometry takes the shapes of equilateral triangles, isosceles trapezoids or parallelograms with internal angles of 60^{o} or 120^{o}.[31] It is noted that the angles are the

same as those between two intersecting zigzag graphene edges, which were proved to be stable under low-voltage electron irradiation by both TEM observations and simulation.[32] Moreover, the nearest-neighbor distance (2.49 Å) in bulk Fe closely matches the periodicity (2.46 Å) of a graphene along the zigzag direction. Therefore, it is not surprising that iron crystals could be embedded into graphene and form epitaxial relation to the zigzag edge, as shown in Fig. 1(a). This atomic model, as optimized in DFT, inspires us the possibility to design a two-dimensional iron crystal with the help of graphene edge. As a comparison, the primitive unit cell is shown in Fig. 1(b), which has a hexagonal symmetry and the lattice constant of 2.42 Å. As the nearest neighbor distance of a 2D iron crystal is close to the periodicity (2.46 Å) along a zigzag graphene edge, the DFT-based structural optimization revealed a perfect epitaxial relation (Fig. 1(a)).

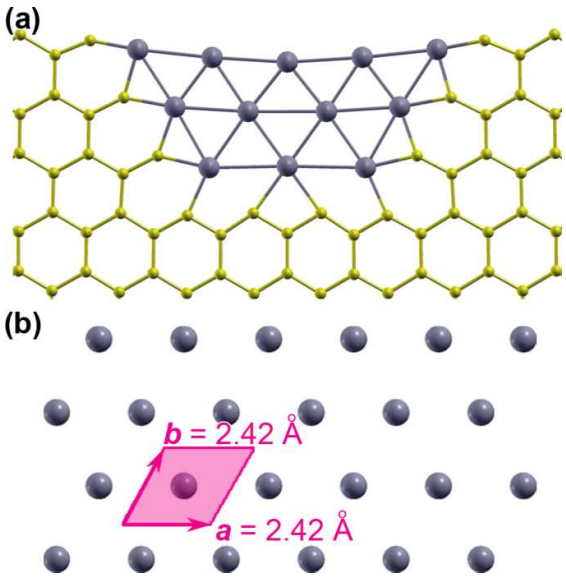

Fig. 1. (a) The DFT-optimized atomic model of a constrained monolayer iron crystals; (b) The shadowed region indicates a 2D primitive unit cell with lattice vectors $a = b = 2.42$ Å and the internal angle of 60°, as optimized by DFT. The large grey dots represent iron atoms.

A series of sandwiched structures were deliberately designed and optimized in DFT to study the constraint effect due to graphene edge. Figure 2(a) shows the relaxed model of a (6, 4) crystal constrained by graphene edges, where (*m*, *n*) denotes a Fe crystal consisting of *m* and *n* repeating cells along vertical and horizontal directions. The equilibrium distance between two boundary Fe atoms is ~ 2.5 Å, which is insensitive to the crystal width. The misfit strain is 1.6% along the boundary. For inner Fe atoms, lateral contraction has been detected for thinner crystals and the inter-distance is ~ 2.36 Å (Fig. 2(b)). When $m > 5$, the Fe-Fe bond length approaches 2.5 Å throughout the structure, indicating a strong constraint effect imposed by the graphene edge. The bonding information is visualized in Fig. 2(c). The edge C-C bonds still preserve the sp^2 character with partial charge transferred to the interface. The unpaired sp^2 electrons are more localized at the interface. The interface is covalently bonded, as indicated by non-negligible charge density of ~ 0.1 e/Bohr^3 in the middle of neighboring Fe and C atoms. The metallic bonding is retained inside the Fe crystal, implied by a homogeneous 2D electron gas.

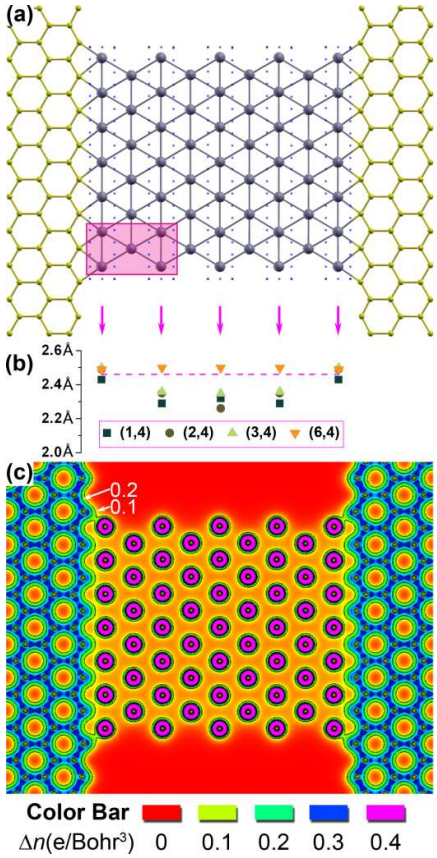

Fig. 2. (a) DFT-relaxed atomic model of a (6, 4) crystal constrained by graphene. The repeating cell is indicated by a shadowed box. (b) The average distance between two neighboring Fe atoms along the vertical direction. The dashed line marks the period of 2.46 Å along the zigzag edge. (c) The charge density contour of a (6, 4) crystal constrained between two graphene strips.

The interfacial strength has been studied by simulating the tension process using the density functional based tight binding method.[24, 25] Figure 3(a) plots the stress-strain curves for 2D Fe crystals in different sizes. The deformation behavior is characterized by an initial elastic response followed by a sudden drop of stress at the nominal strain ~ 10%, indicating a structural change. A close observation shows that the Fe crystal lattice curved toward the center and the width decreased under tension. At a threshold strain, the 2D lattice collapsed into locally close-packed structures

(insets to Fig. 3(a)). Figure 3 (b) and (c) reveal that the strain is more localized in the Fe region. The severe distorted region is located at the boundary, which mitigated the constraint from graphene edge and finally led to reconstruction. The observation clearly indicates that the structural stability is closely related to the edge constraint. The interfacial strength increases with the crystal width and reaches ~ 20 GPa for the (5, 3) crystal. For thinner crystals, continuous reconstruction transforms the planar configuration into a wired structure after yielding, leading to larger failure strains.

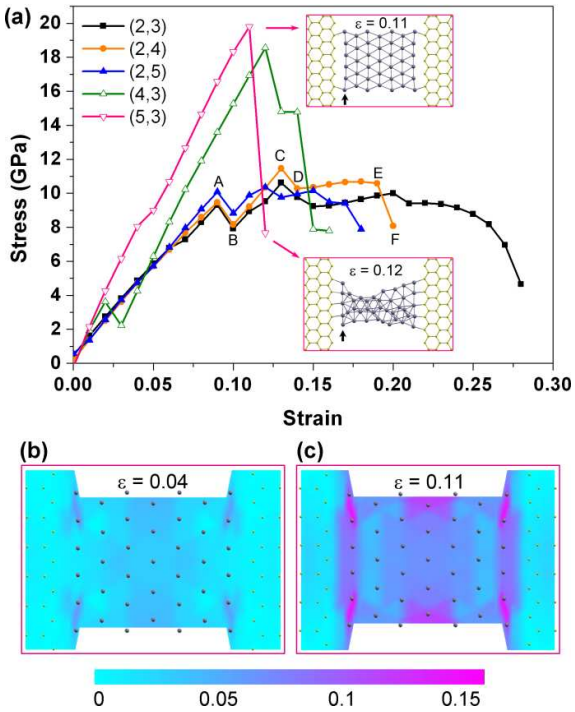

Fig. 3. (a) The stress-strain curves for 2D Fe crystals with different sizes. Insets are the corresponding atomic structures before and after structural collapse. (b) and (c) are the longitudinal strain mappings of a (5, 3) crystal at nominal strains of 0.04 and 0.11, respectively.

B. Electronic and magnetic structure of a monolayer iron crystal

Figure 1 suggests three possible prototypes of graphene-metal contacts, termed type I, II and III, respectively, as shown in Fig. 4. The 2D iron crystal remains metallic in all three models. The type-I and II models have the boundary Fe atoms aligned to the valleys and the peaks of the zigzag graphene edge, respectively. The corresponding Fe-C bond lengths are 2.09 Å and 1.93 Å. The graphene edge is nearly intact, as shown by the preserved sp^2 characters of the C-C bonding. For the type-III model, the Fe atoms replace the outmost C atoms along the zigzag edge and form stronger covalent bonds with a length of 1.85 Å. The binding energies per boundary Fe atom for three models are 5.31 eV, 4.79 eV and 8.45 eV, respectively.

The charge redistribution (Fig. 4) upon formation of the 1D metal-graphene interface can be visualized by the plane-averaged electron density,[33, 34] *i.e.*

$$\Delta n(x) = n_{\mathrm{G|M}}(x) - n_{\mathrm{G}}(x) - n_{\mathrm{M}}(x)$$

where $n_{\mathrm{G|M}}(x)$, $n_{\mathrm{G}}(x)$ and $n_{\mathrm{M}}(x)$ denote the plane-averaged densities of the graphene-metal interface, only the graphene part, and only the 2D Fe crystal part, respectively. The net transferred charges per boundary Fe atom are 0.10 e, 0.14 e and 0.20 e, respectively, for the three cases. It is noted that, for type-I and II models, the transferred charge is mainly located in the middle of Fe-C bonds, while it is much closer to the C center for type-III model. Based on the projected DOS analysis, the charge transfer is a direct consequence of the orbital hybridization between the graphene and the iron crystal. The hybridized orbitals of C atoms are 2*s* and 2*px* for type-I and -II models, and 2*s* and 2*py* for type-III model. The charge transfer is also consistent with the calculated work functions. The work function of the 2D iron

crystal is 4.1 eV along <110> direction, which is lower than the corresponding work functions of graphene along the same direction in Fig. 4(b) and (c) (4.7 eV and 6.6 eV, respectively).

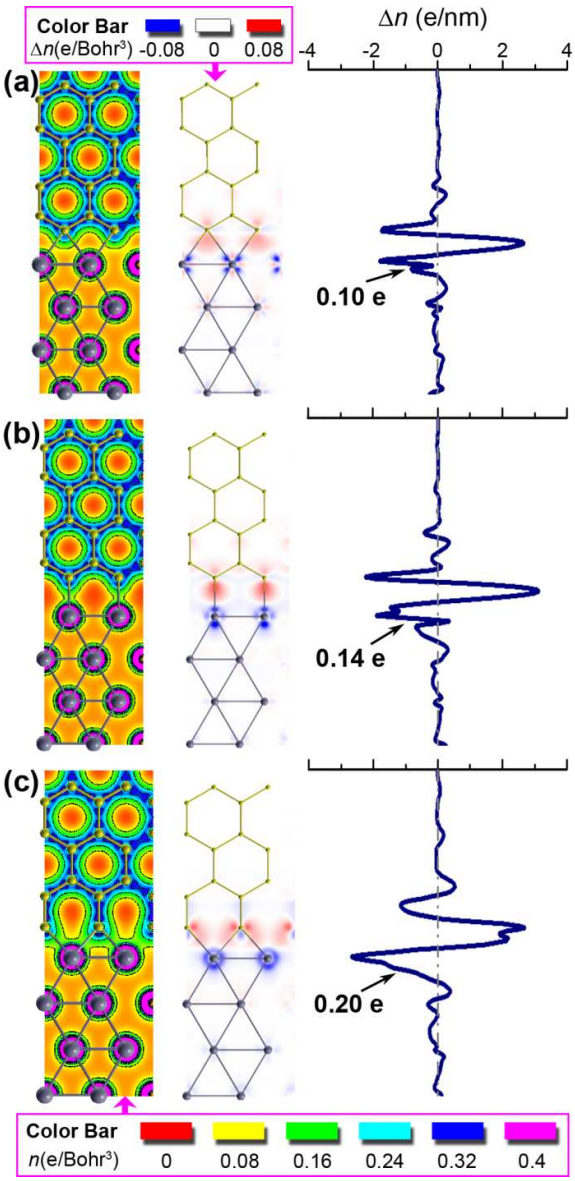

Fig. 4. Contour plots of charge density (left), the density of electron difference upon formation of the interfaces (middle) and the corresponding plane-averaged electron density per unit cell (right) for (a) type-I, (b) type-II and (c) type-III models.

Figure 5 plots the spatial distribution of spin polarization density for three 1D contacts. The magnetic moment of a free zigzag graphene edge is 1.3 μ_B, as is contributed by the unpaired σ electrons (1 μ_B) and the edge-localized π-orbitals (~ 0.3 μ_B). For both type-I and II models, the local magnetic moment of the edge C atoms is greatly reduced due to the formation of covalent bonds. The PDOS analysis reveals that the major character of the exchange splitting in π-orbital states in a free zigzag edge preserves in both models. The remnant magnetic moment, however, depends on the specific interface structures. For type-I model, the communication in free electrons shifts the Fermi energy to the majority spin states, being parallel to that of the ferromagnetic 2D Fe crystal, which explains the small remnant magnetic moment of the edge C atoms. On the other hand, the spin polarization near the Fermi energy is substantially enhanced, implying larger conductance of electrons with majority spins in the graphene region. In contrast, the 2D Fe crystal in type-II model has less effect on the adjacent graphene support, as revealed by the remnant magnetic moment (-0.24 μ_B) and the resemblance of the PDOS at edge C sites in both type-II model and a free zigzag edge. For type-III model, both spin-up and spin-down π-orbital states are suppressed near the Fermi energy, indicating a poor interfacial conductance. The remnant magnetic moment is contributed by both σ and π electrons.

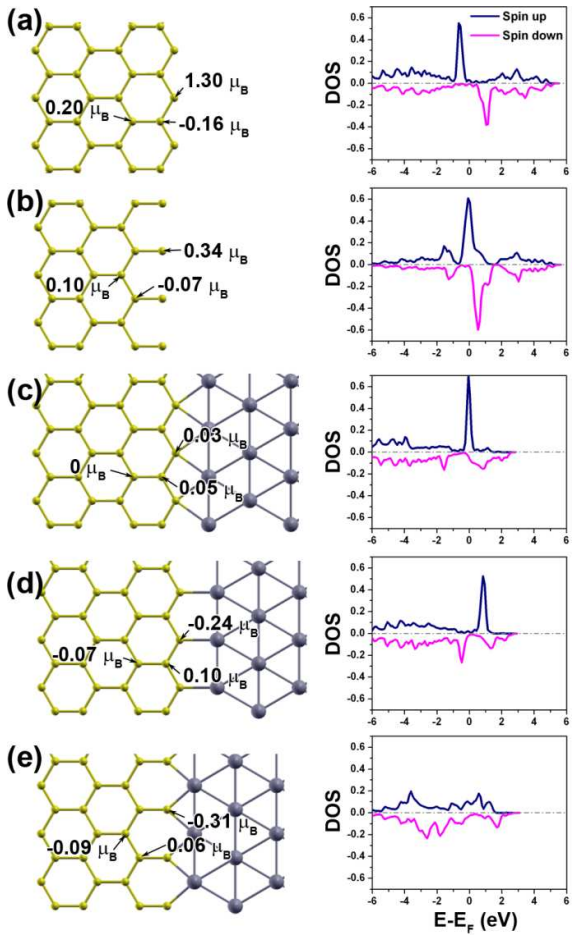

Fig. 5. The magnetic moments (left) and the projected DOS of π-orbital of edge C atoms (right) on the boundary of (a) a free graphene zigzag edge, (b) a modified graphene edge, (c) type-I, (d) type-II and (e) type-III junction models.

As a direct consequence of the lower dimensionality, the magnetic moment is increased to 2.68 μB/atom for the monolayer crystal, as compared to its bulk counterpart (2.2 μB/atom). The 2D feature reduces the overlap of 3*d* orbitals along the normal to the crystal plane (*i.e. z*-axis). Accordingly, the $3dz^2$ orbital has a relatively flat band and shows isolated peaks in the PDOS (Fig. 6). On the other hand, localization of the 3*d* electrons in the crystal plane leads to shorter neighboring distance, and consequently denser in-plane orbital overlaps. As compared to the $3dz^2$

orbital, the 3*dzx* and 3*dzy* orbitals have more complex band structure and wider distribution of PDOS. The most severe splitting is observed in the PDOS of the $3dx^2$-y^2 and 3*dxy* orbitals (Fig. 6), which subsequently affects spin polarization. The $3dz^2$ orbital is mainly occupied by the majority spin electron, while the severe splitting in $3dx^2$-y^2 and 3*dxy* orbitals reduces the occupation difference between the spin-up and spin-down electrons. For the 4*s* orbital, in-plane localization leads to isolated peaks distributed in a wide energy range. The contribution to the magnetic moment is 0.84 μB for the $3dz^2$ orbital, 0.54 μB for both $3dx^2$-y^2 and 3*dxy* orbitals and 0.40 μB for both $3dx^2$-y^2 and 3*dxy* orbitals.

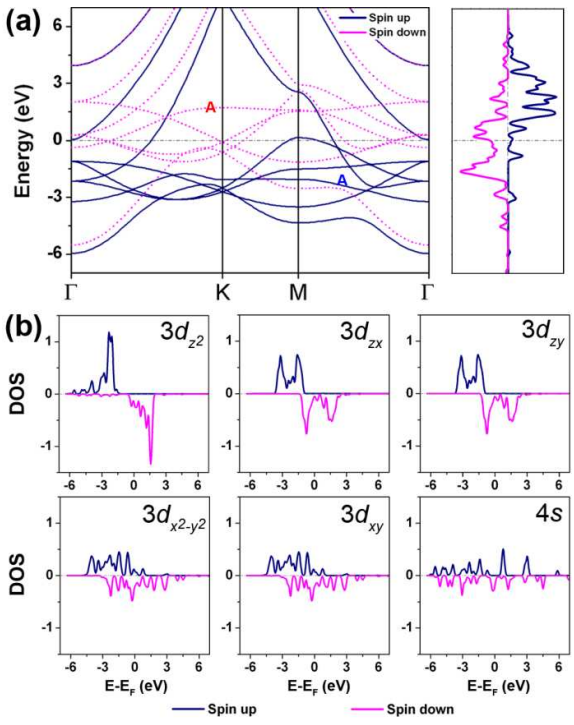

Fig. 6. (a) Band structure and DOS of a monolayer iron crystal; (b) The projected DOS of $3dz^2$, 3*dzx*, 3*dzy*, $3dx^2$-y^2, 3*dxy* and 4*s* of a Fe atom in the monolayer iron crystal.

The magnetic structures were investigated based on the total energy calculation.

Three states with different spin configurations have been considered, *i.e.* FM, AFM and AFM_2 in Fig. 7(a), among which the FM state has the lowest energy. Taking a graphene-constrained (2, 3) crystal as an example, one finds that AFM and AFM_2 states have the energy differences of 3.6 eV and 5.0 eV to the FM state, respectively. The total energy calculation was performed on the same-sized planar crystal without constraint so as to examine the contribution from graphene. The energy differences were found to be 1.3 eV and 2.1 eV. Clearly, the presence of the graphene constraint greatly stabilizes the FM state. The reduced coordination number causes more localized 3*d* electrons, as observed in other low-dimensional Fe structures, such as atomic chains or small clusters.[35] The majority spin band is fully occupied, giving an average magnetic moment of 2.68 μ_B for Fe atoms. Figure 7(b) plots the spatial distribution of spin polarization density in both the graphene strips and the planar Fe crystal. At the free graphene edge, the magnetic moment (~1 μ_B) is mainly contributed by the unpaired σ electrons. The edge-localized π-orbitals lead to magnetic tails (~0.25 μ_B) extended into the sub-edge region, as indicated by letter A. In contrast, the magnetic moment at the junction (region B) vanishes due to the shift of Fermi energy.

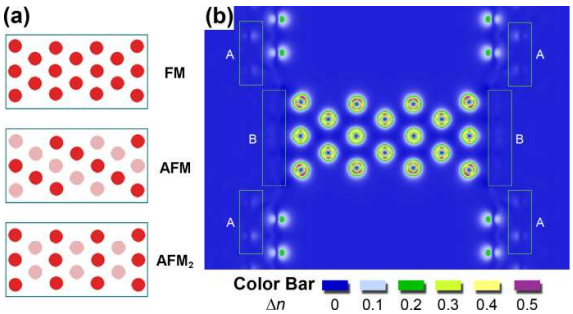

Fig. 7. (a) Three magnetic states with different spin ordering of a (2, 3) crystal: FM denotes ferromagnetically ordered spins; AFM and AFM_2 denote antiferromagnetical states with opposite

spins ordered in two different configurations; (b) The spatial distribution of the spin polarization density of the FM state.

C. Improved stability of a bilayer iron crystal

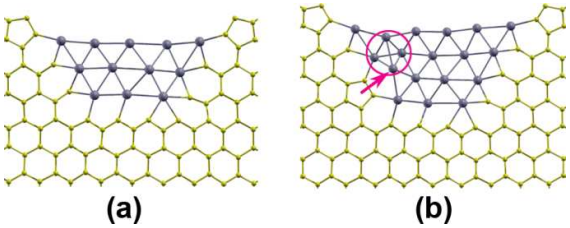

FIG. 8. (a) Configuration of an embedded monolayer iron crystal after MD/DFTB relaxation for 10 ps at room temperature. (b) The destruction of a slightly larger monolayer crystal initiates at 0.6 ps during relaxation at room temperature. The arrow indicates that an iron atom is detached from the interface to form a local tetrahedron, marked by a circle.

Room temperature stability of the 2D iron crystals has been studied by the MD/DFTB method. In the absence of constraint, monolayer iron crystals would collapse into a spherical cluster rapidly after relaxation. By embedding a small crystal into the graphene edge (Fig. 8(a)), it retains the 2D structure after the room-temperature relaxation. However, we observed quick destruction of a similar 2D configuration with a slightly larger size under the same condition (Fig. 8(b)). The iron atom, as indicated by the arrow, moves out of the atomic plane and forms a locally close-packed structure with neighboring atoms, as marked by a circle. By lowering MD temperatures, larger constrained 2D iron crystals can be attained in simulations. The poor stability explains the rare observations of free-standing 2D metal structures.

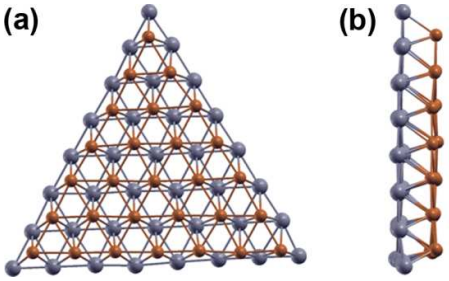

Fig. 9. (a) Front and (b) side views of a bilayer iron crystal, taking a planar shape of equilateral triangle, after MD/DFTB relaxation at room temperature.

On the contrary, recent study by Wang *et al.* revealed surprising stability of a 2D bilayer iron crystal on the graphene surface with a close-packed stacking.[31] Figure 9(a) shows a typical bilayer crystal without constraints. During the whole MD/DFTB simulation period of 10 ps, only edge atoms were discernibly deviated from the original locations due to their less coordination (Fig. 9), while all surface atoms remained in position. The bilayer crystal retained its shape for longer simulation periods at room temperature and melt into a spherical cluster only at high temperatures, *e.g.* 800 K for a 2 nm bilayer crystal, demonstrating better stability than its monolayer counterpart. It is noted that a cluster in equiaxial shapes may attain lower energy due to the smaller surface areas. However, the basal plane of a close-packed structure has the lowest specific surface energy. In order to displace an atom from its in-plane location, an activation energy barrier is encountered. The latter may explain the observed stability in both experiments[31] and simulations.

IV. CONCLUSIONS

In summary, DFT-based simulations show the possibility of epitaxial growth of 2D iron crystals on graphene edges, which provide effective constraints hindering the transformation into 3D structures. Both the electronic structure and the magnetic

property show a strong correlation to the dimensionality. The magnetic moment is increased to be 2.68 μB/atom by lowering the dimension from 3D to 2D. The one-dimensional coherent interface makes perfect 1D contact between 2D crystals with different bonding natures, which differs from the interfaces in the stacking graphene heterostructure. From the strong support from the non-magnetic graphene, it is possible to construct a 2D device prototype, which may have potential applications in 2D spintronics.[36, 37] As dimensionality has been demonstrated as the most fascinating parameter in changing the material properties, this 1D contact is expected to behave differently from its 2D counterparts, and certainly deserves further investigation.

ACKNOWLEDGMENTS

H Wang acknowledges the financial support from the National Science Foundation of China (Grant No. 11322219; Grant No.11321202). We acknowledge the TEM work performed in the Imaging and Characterization Core Lab of King Abdullah University. The computational work carried out by TianHe-1(A) system at National Supercomputer Center in Tianjin is gratefully acknowledged.

REFERENCES

1. K. Nakada, M. Fujita, G. Dresselhaus and M. S. Dresselhaus, *Phys. Rev. B*, 1996, **54**, 17954.

2. Y.-W. Son, M. L. Cohen and S. G. Louie, *Nature*, 2006, **444**, 347-349.

3. K. A. Ritter and J. W. Lyding, *Nat. Mater.*, 2009, **8**, 235-242.

4. M. Acik and Y. J. Chabal, *Jpn. J. Appl. Phys.*, 2011, **50**, 070101.

5. X. Jia, J. Campos-Delgado, M. Terrones, V. Meunier and M. S. Dresselhaus, *Nanoscale*, 2011, **3**, 86-95.

6. O. V. Yazyev and M. I. Katsnelson, *Phys. Rev. Lett.*, 2008, **100**, 047209.

7. R. Sharma, J. H. Baik, C. J. Perera and M. S. Strano, *Nano Lett.*, 2010, **10**, 398-405.

8. L. D. Landau, *Phys. Z. Sowjetunion*, 1937, **11**, 26-25.

9. R. E. Peierls, *Helv. Phys. Acta*, 1934, **7**, 81-83.

10. J. C. Meyer, A. K. Geim, M. I. Katsnelson, K. S. Novoselov, T. J. Booth and S. Roth, *Nature*, 2007, **446**, 60-63.

11. N. D. Mermin, *Phys. Rev.*, 1968, **176**, 250-254.

12. K. S. Novoselov, D. Jiang, F. Schedin, T. J. Booth, V. V. Khotkevich, S. V. Morozov and A. K. Geim, *P. Natl. Acad. Sci. USA* 2005, **102**, 10451-10453.

13. B. Lalmi, H. Oughaddou, H. Enriquez, A. Kara, S. Vizzini, B. Ealet and B. Aufray, *Appl. Phys. Lett.* , 2010, **97**, 223109-223102.

14. P. Vogt, P. De Padova, C. Quaresima, J. Avila, E. Frantzeskakis, M. C. Asensio, A. Resta, B. Ealet and G. Le Lay, *Phys. Rev. Lett.*, 2012, **108**, 155501.

15. P. A. Thiel, M. Shen, D.-J. Liu and J. W. Evans, *J. Phys. Chem. C*, 2009, **113**, 5047-5067.

16. A. T. N'Diaye, S. Bleikamp, P. J. Feibelman and T. Michely, *Phys. Rev. Lett.*, 2006, **97**, 215501.

17. J. M. Wen, S. L. Chang, J. W. Burnett, J. W. Evans and P. A. Thiel, *Phys. Rev. Lett.*, 1994, **73**, 2591-2594.

18. Z. Liu, L. Song, S. Zhao, J. Huang, L. Ma, J. Zhang, J. Lou and P. M. Ajayan, *Nano*

Lett. , 2011, **11**, 2032-2037.

19. L. A. Ponomarenko, A. K. Geim, A. A. Zhukov, R. Jalil, S. V. Morozov, K. S. Novoselov, I. V. Grigorieva, E. H. Hill, V. V. Cheianov, V. I. Fal'ko, K. Watanabe, T. Taniguchi and R. V. Gorbachev, *Nat Phys*, 2011, **7**, 958-961.

20. G. Paolo, B. Stefano, B. Nicola, C. Matteo, C. Roberto, C. Carlo, C. Davide, L. C. Guido, C. Matteo, D. Ismaila, C. Andrea Dal, G. Stefano de, F. Stefano, F. Guido, G. Ralph, G. Uwe, G. Christos, K. Anton, L. Michele, M.-S. Layla, M. Nicola, M. Francesco, M. Riccardo, P. Stefano, P. Alfredo, P. Lorenzo, S. Carlo, S. Sandro, S. Gabriele, P. S. Ari, S. Alexander, U. Paolo and M. W. Renata, *J. Phys-Condens. Mat.*, 2009, **21**, 395502.

21. H. J. Monkhorst and J. D. Pack, *Phys. Rev. B*, 1976, **13**, 5188-5192.

22. A. M. Rappe, K. M. Rabe, E. Kaxiras and J. D. Joannopoulos, *Phys. Rev. B*, 1990, **41**, 1227-1230.

23. J. P. Perdew, K. Burke and M. Ernzerhof, *Phys. Rev. Lett.*, 1996, **77**, 3865-3868.

24. M. Elstner, D. Porezag, G. Jungnickel, J. Elsner, M. Haugk, T. Frauenheim, S. Suhai and G. Seifert, *Phys. Rev. B*, 1998, **58**, 7260-7268.

25. B. Aradi, B. Hourahine and T. Frauenheim, *J. Phys. Chem. A*, 2007, **111**, 5678-5684.

26. Y. Ohta, Y. Okamoto, S. Irle and K. Morokuma, *Carbon*, 2009, **47**, 1270-1275.

27. Y. Ohta, Y. Okamoto, S. Irle and K. Morokuma, *J. Phys. Chem. C*, 2008, **113**, 159-169.

28. Y. Ohta, Y. Okamoto, S. Irle and K. Morokuma, *ACS Nano*, 2008, **2**, 1437-1444.

29. Y. Ohta, Y. Okamoto, S. Irle and K. Morokuma, *Phys. Rev. B*, 2009, **79**, 195415.

30. Y. Ohta, Y. Okamoto, A. J. Page, S. Irle and K. Morokuma, *ACS Nano*, 2009, **3**, 3413-3420.

31. H. Wang, K. Li, Y. Yao, Q. Wang, Y. Cheng, U. Schwingenschlögl, X. X. Zhang and W. Yang, *Sci. Rep.*, 2012, **2**, 995.

32. Ç. Ö. Girit, J. C. Meyer, R. Erni, M. D. Rossell, C. Kisielowski, L. Yang, C.-H. Park, M. F. Crommie, M. L. Cohen, S. G. Louie and A. Zettl, *Science*, 2009, **323**, 1705-1708.

33. G. Giovannetti, P. A. Khomyakov, G. Brocks, V. M. Karpan, J. van den Brink and P. J. Kelly, *Phys. Rev. Lett.*, 2008, **101**, 026803.

34. P. A. Khomyakov, G. Giovannetti, P. C. Rusu, G. Brocks, J. van den Brink and P. J.

Kelly, *Phys. Rev. B*, 2009, **79**, 195425.

35. I. M. L. Billas, J. A. Becker, A. Châtelain and W. A. de Heer, *Phys. Rev. Lett.*, 1993, **71**, 4067-4070.

36. R. Jansen, *J. Phys. D-Appl. Phys.*, 2003, **36**, R289-R308.

37. S. Sugahara and J. Nitta, *Proc. IEEE*, 2010, **98**, 2124-2154.